

THE COMPLETE NATURE OF THE WARM DUST SHELL IN PERSEUS

NAOMI A. RIDGE, SCOTT L. SCHNEE, ALYSSA A. GOODMAN, AND JONATHAN B. FOSTER

Harvard-Smithsonian Center for Astrophysics, 60 Garden Street, Cambridge, MA 02138; nr ridge@cfa.harvard.edu, sschnee@cfa.harvard.edu, agoodman@cfa.harvard.edu

Received 2005 April 28; accepted 2006 January 19

ABSTRACT

The Perseus molecular cloud complex is a $\gtrsim 30$ pc long chain of molecular clouds most well known for the two star-forming clusters NGC 1333 and IC 348 and the well-studied outflow source in B5. However, when studied at mid- to far-infrared wavelengths, the region is dominated by a ~ 10 pc diameter shell of warm dust, likely generated by an H II region caused by the early-B star HD 278942. Using a revised calibration technique the COMPLETE team has produced high-sensitivity temperature and column density maps of the Perseus region from *IRAS* Sky Survey Atlas (ISSA) 60 and 100 μm data. In this paper, we combine the ISSA-based dust-emission maps with other observations collected as part of the COMPLETE Survey, along with archival H α and *MSX* observations. Molecular line observations from FCRAO and extinction maps constructed by applying the NICER method to the 2MASS catalog provide independent estimates of the “true” column density of the shell. H α emission in the region of the shell confirms that it is most likely an H II region located behind the cloud complex, and 8 μm data from *MSX* indicate that the shell may be interacting with the cloud. Finally, the two polarization components seen toward background stars in the region by Goodman et al. can be explained by the association of the stronger component with the shell. If confirmed, this would be the first observation of a parsec-scale swept-up magnetic field.

Subject headings: dust, extinction — H II regions — infrared: ISM — ISM: individual (G159.6-18.5) — radio lines: ISM

Online material: color figure

1. INTRODUCTION

The interaction of newly formed stars with their parent cloud, particularly in the case of massive stars, can have significant consequences for the subsequent development of the cloud. Hot, massive stars will cause cloud disruption through their ionizing flux, as well as through the momentum in their stellar winds. Alternatively, given the right conditions in the cloud, stellar winds may also trigger the collapse of cloud cores and induce further star formation.

One region where a stellar wind may be triggering star formation is the Perseus molecular cloud complex, a well-studied chain of molecular clouds extending approximately 30 pc in length. The complex has a total mass of $\sim 1.3 \times 10^4 M_\odot$, assuming it is at a distance of 260 pc (although actual distance estimates range from 230 pc [Černis 1990] to 350 pc [Herbig & Jones 1983], and it is clear from the large $[\gtrsim 10 \text{ km s}^{-1}]$ velocity range of molecular gas that a single distance to the entire complex is unlikely). Star formation is ongoing in several parts of the complex, most obviously around the two reflection nebulae IC 348 and NGC 1333. Several surveys (e.g., Ladd et al. 1993; Aspin et al. 1994; Lada & Lada 1995; Luhman et al. 2003) have established that there is a population of pre-main-sequence stars located both within the clusters and throughout the complex, but relatively few high-mass stars have been found.

The Perseus complex is not just interesting for its star-forming properties. An almost complete shell of enhanced emission can be seen in *Infrared Astronomical Satellite* (*IRAS*) data toward the center of the molecular cloud complex (Fig. 1). The shell, referred to in previous papers as G159.6-18.5, has a diameter of 0.75° , or 10 pc at the distance of the molecular cloud. Although its existence has been known for about 15 years (it was first described by Pauls & Schwartz [1989] in a conference proceeding and further discussed by Fiedler et al. [1994]), there has been little investigation into the nature or source of the shell, and it has been mostly ignored by studies of star formation in the region.

Based on radio data, Fiedler et al. argued that the feature is caused by a supernova remnant, which if true would be one of the closest to the Sun, and has the highest known Galactic latitude for such an object. More recently, de Zeeuw et al. (1999) associated the shell with the B star HD 278942, located at its geometric center. Andersson et al. (2000) performed a multiwavelength study of the star and its surroundings. They reclassified HD 278942 as an O9.5–B0 V star with an age of 8 Myr and found weak radio-continuum emission with a flat spectral index, consistent with an optically thin H II region filling the shell. However, partly due to the lack of short-spacing information in their interferometer maps leading to large uncertainties on the derived radio-continuum fluxes, they could not rule out a negative spectral index, leaving the possibility that the radio continuum is due to synchrotron emission from the interaction between a stellar wind or supernova remnant and the molecular cloud. Andersson et al.’s other observations concentrated on the central star HD 278942 and hence provide little insight into the nature of the shell itself.

The Perseus molecular cloud complex is a target of the *Spitzer Space Telescope* Legacy program From Molecular Cores to Planet Forming Disks (hereafter c2d; Evans et al. 2003), while the two clusters NGC 1333 and IC 348 are included in a *Spitzer* Guaranteed Time Observer (GTO) program. These programs aim to determine the distribution of young stars and clusters and investigate their association with known dense cores. The ongoing COMPLETE¹ Survey (Ridge et al. 2006) is a large international effort that has coordinated its observations with c2d. COMPLETE aims to obtain and compare high-quality molecular line, submillimeter continuum, far-infrared column density, and near-infrared extinction data over the extents of three of the star-forming molecular clouds targeted by c2d, including the whole of Perseus.

¹ Coordinated Molecular Probe Line Extinction and Thermal Emission; <http://cfa-www.harvard.edu/COMPLETE>.

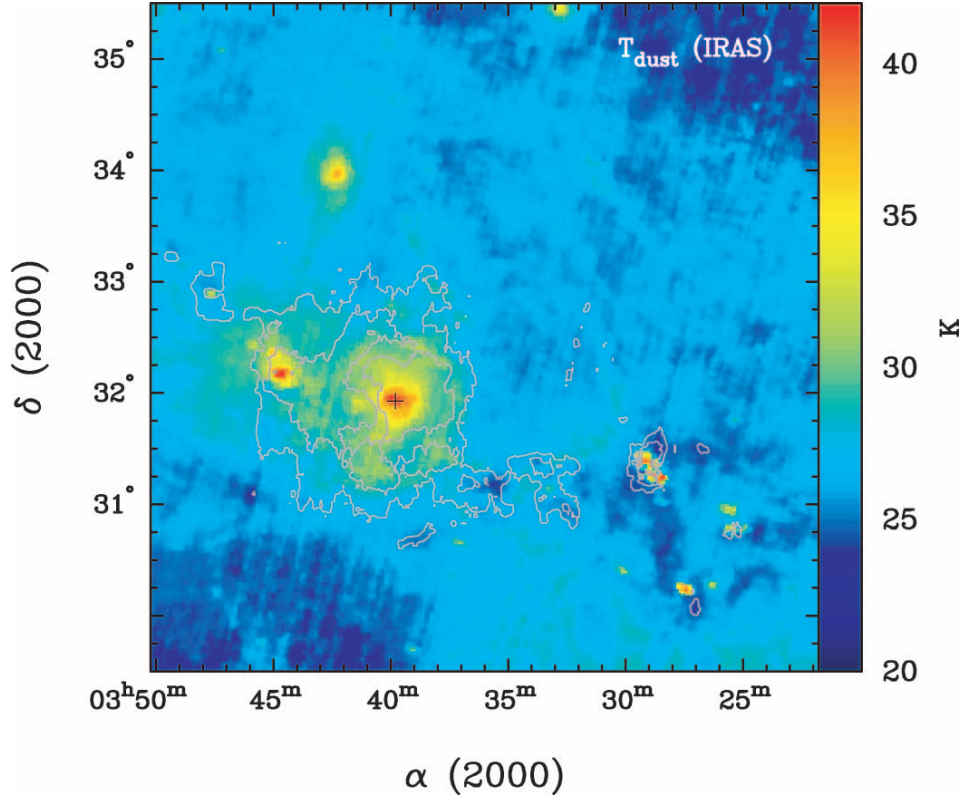
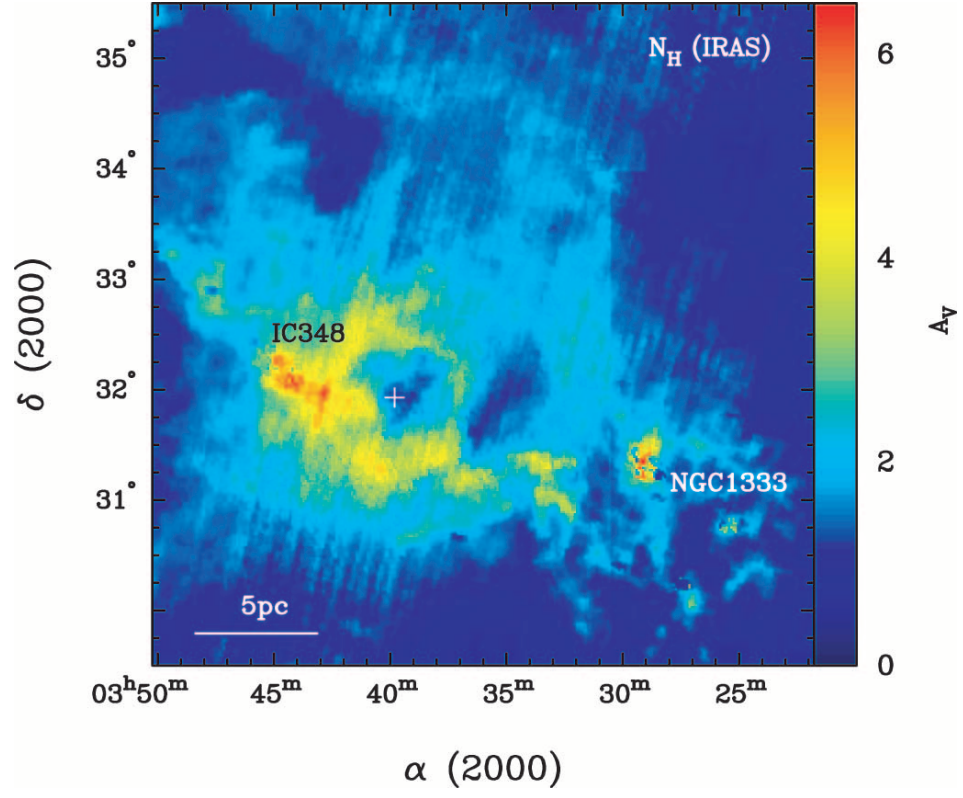


FIG. 1.—Column density in units of A_V derived from *IRAS* 60 and 100 μm emission (*top*) and temperature overlaid with contours of column density (*bottom*), in the direction of the Perseus molecular cloud complex. The position of the well-known star-forming clusters NGC 1333 and IC 348 are shown for orientation. A bright shell of emission, filled with warm material, dominates the region at these wavelengths. The plus sign indicates the position of the B star HD 278942, which has been proposed as the progenitor of the shell.

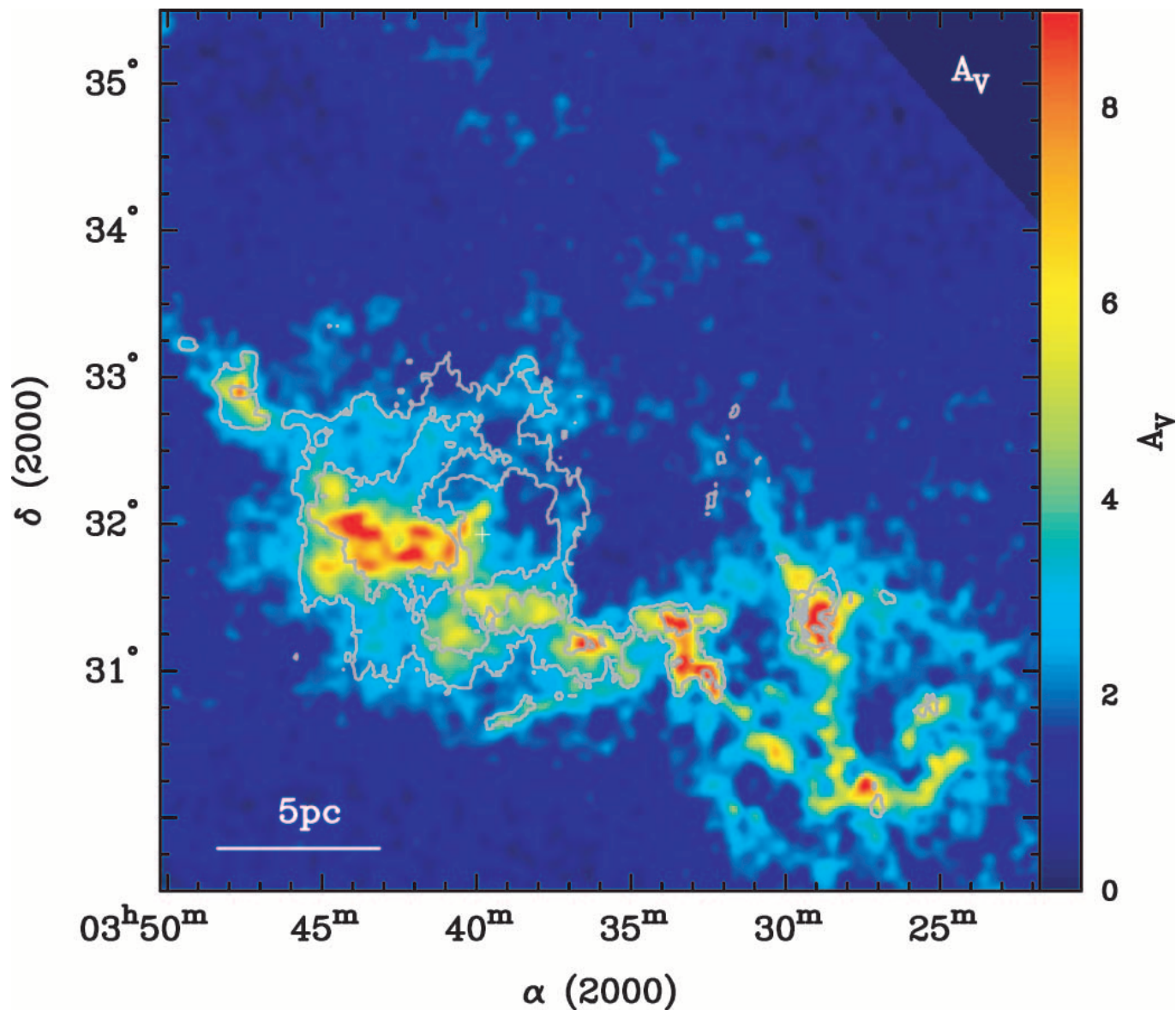


FIG. 2.—Color: Near-IR-based extinction map of Perseus, covering the same area shown in Fig. 1. This map was constructed by applying the NICER algorithm to data from the 2MASS catalog. Again, the plus sign indicates the position of HD 278942. Contours: *IRAS* column density (levels are $A_V = 2.5, 3.5$). From Ridge et al. (2006).

As part of COMPLETE, we have recently used 60 and 100 μm *IRAS* maps of the Perseus region to create new high-sensitivity temperature and column density maps (Schnee et al. 2005). Here we intercompare the recalibrated far-IR results with COMPLETE near-infrared extinction and ^{13}CO maps of the same region (Ridge et al. 2006), an $\text{H}\alpha$ image from the VTSS² Survey, and the *Midcourse Space Experiment* (*MSX*) 8 μm image. A detailed picture of the shell, which would not be possible by looking at each data set alone, emerges and suggests a complex picture of Perseus as a group of cold molecular clouds being impacted gently from behind by a stellar wind bubble.

2. DATA AND ANALYSIS

2.1. *IRAS* Temperature and Column Density Maps

Figure 1 shows maps of color temperature and column density in Perseus from Schnee et al. (2005). These were constructed from

recalibrated 60 and 100 μm *IRIS*³ images (Miville-Deschênes & Lagache 2005). These data provide excellent correction for the effects of zodiacal dust and striping in the *IRAS* images and improved gain, offset, and zero-point calibration over earlier releases of the *IRAS* data (Schnee et al. 2005). Near-infrared extinction maps (see § 2.2) were used to constrain the conversion factor between 100 μm optical depth and visual extinction (column density), as using the “standard” values for this conversion (e.g., Wood et al. 1994) results in a significant miscalculation of the extinction (Schnee et al. 2005). Hence, these maps provide the best dust-temperature and extinction maps constructed from *IRAS* data to date.

The positions of the well-known star-forming clusters NGC 1333 and IC 348 are indicated in Figure 1. The shell is clearly seen as an enhancement in column density and is filled with warm material, evident in the temperature map. Although on careful inspection the known dark cores in Perseus are visible in the

² Virginia Tech Spectral-Line Survey; <http://www.phys.vt.edu/~halph/>.

³ Improved Recalibration of the *IRAS* Survey.

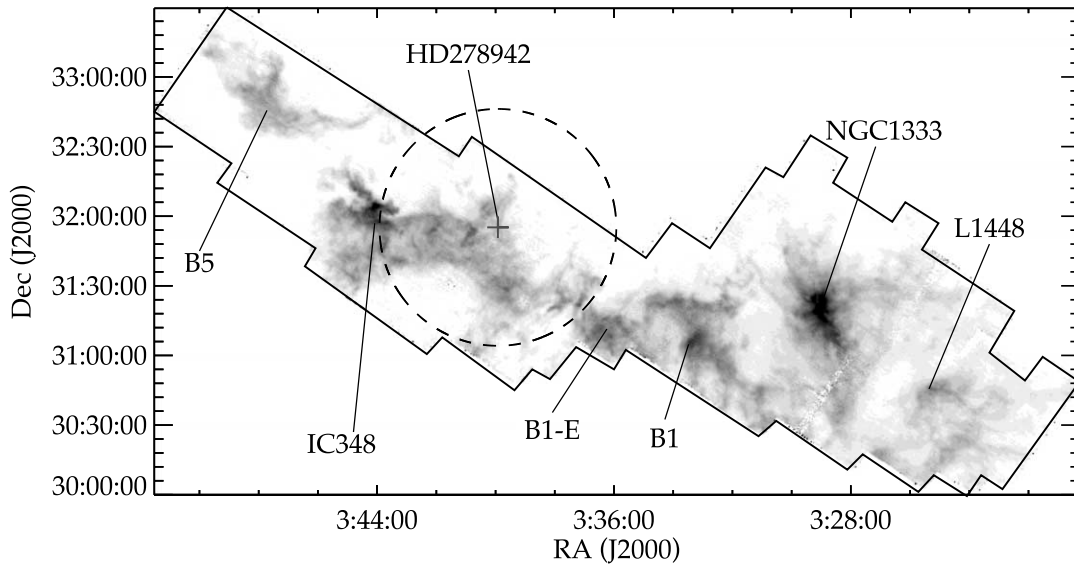


FIG. 3.—“Traditional” picture of Perseus; a chain of molecular clouds shown in ^{13}CO integrated intensity. The solid black line shows the border of the observed region. The plus sign indicates the position of HD 278942, and the locations of well-known star-forming sites are indicated. This map does not extend significantly into the area of the shell (shown by the dashed circle), but there is no hint of its existence from the ^{13}CO integrated emission. From Ridge et al. (2006). [See the electronic edition of the *Journal* for a color version of this figure.]

map, the general morphology (dominated by the shell) is very different from extinction or molecular line maps of the region, which are dominated by the chain of clouds (see §§ 2.2 and 2.3).

2.2. Extinction from Near-Infrared Color Excess

As part of COMPLETE, we have constructed a map of the extinction toward Perseus with comparable resolution ($5'$) to the $4'/7$ *IRAS*-based maps by applying the NICER⁴ algorithm (Lombardi & Alves 2001) to data from the Two Micron All Sky Survey (2MASS; Ridge et al. 2006). This method uses the near-infrared color excess of background stars to determine reddening along a line of sight and hence does not rely on assumptions about grain-size distribution or emissivity. The extinction determined in this way should therefore provide the best measure of the true column density distribution of material (A. A. Goodman et al. 2006, in preparation). The 2MASS/NICER extinction map is shown in Figure 2. Here the more familiar view of Perseus as a chain of molecular clouds—from B5 in the northeast through IC 348, B1, and NGC 1333 in the southwest—is clearly visible. The position of HD 278942 is indicated by a plus sign, and although faint, the northern half of the shell, centered on the star, can be made out in the image.

2.3. Molecular Line Emission from ^{13}CO

A map of ^{13}CO integrated intensity (representing gas column density) with $44''$ resolution, obtained for COMPLETE at the Five College Radio Astronomy Observatory (FCRAO) 14 m telescope, is shown in Figure 3. A full description of the data acquisition and reduction methods is given in Ridge et al. (2006).

Although not as extensive as the *IRAS* and 2MASS/NICER images, the higher resolution of this map reveals significant substructure when compared to those images.⁵ Like the 2MASS/

NICER extinction map, the ^{13}CO integrated intensity shows the familiar chain of molecular clouds, with no hint of the existence of the warm dust shell so clear in the *IRAS*-based image.

2.4. $\text{H}\alpha$ Image from VTSS

Figure 4 shows a $3^\circ \times 3^\circ$ $\text{H}\alpha$ image centered on $\alpha = 03^{\text{h}}39^{\text{m}}57^{\text{s}}.1$, $\delta = +31^\circ55'15''$ obtained via SkyView from the VTSS, overlaid with contours of *IRAS* column density. The image has a resolution of $6'$.

There is clearly ionized gas filling the shell, indicating that it is likely to be an H II region or stellar wind. The $\text{H}\alpha$ emission displays three distinct peaks, the brightest to the northeast. The substructure in the $\text{H}\alpha$ emission, in particular the apparent lack of emission to the southeast, is discussed in § 3.2.

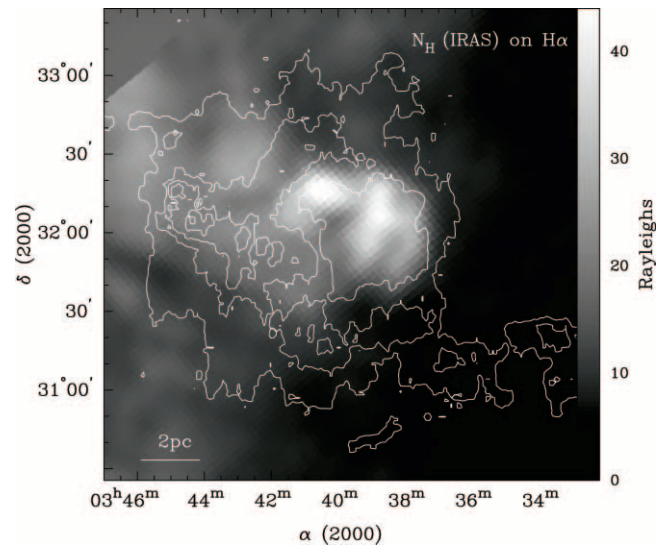


FIG. 4.— $\text{H}\alpha$ emission (Finkbeiner 2003; Dennison et al. 1998), overlaid with contours of N_{H} (in units of A_V) from *IRAS*. $\text{H}\alpha$ emission fills the shell, indicating that it is likely to be an H II region or stellar wind.

⁴ Near-Infrared Color Excess Revisited.

⁵ Figure reproductions presented here do not allow for the reader to see the full detail of the map; higher resolution versions and the raw data are available at <http://cfa-www.harvard.edu/COMPLETE>.

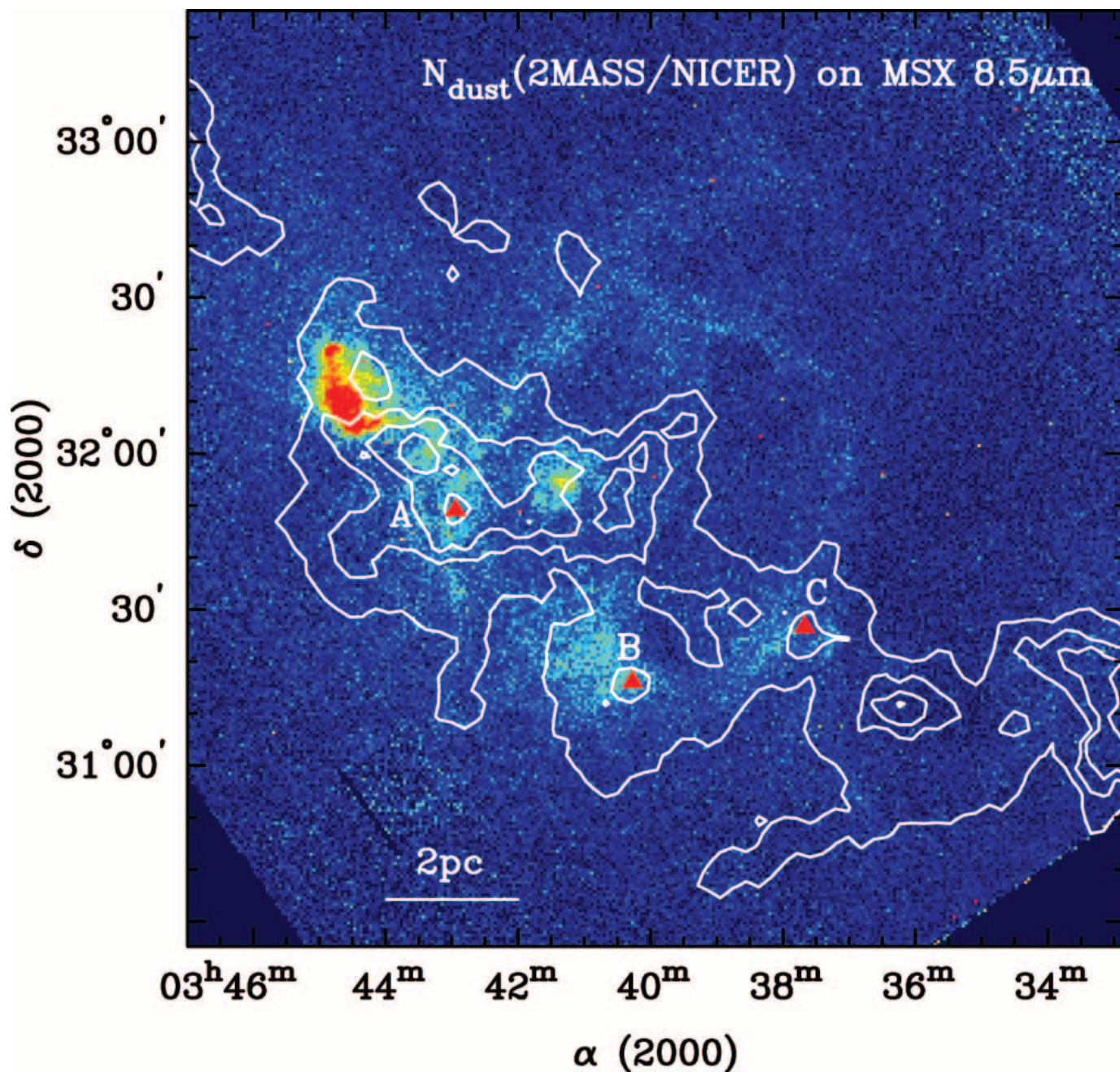


FIG. 5.—*MSX* 8 μm image of the shell, overlaid with contours of extinction (from 2MASS/NICER). Contour levels start at an A_V of 3 and increase in increments of 2. The bright 8 μm “knots,” indicated by red triangles and labeled A, B, and C, are spatially coincident with enhancements in the extinction. ^{13}CO spectra at these positions are shown in Fig. 14 and discussed in § 3.3.

2.5. Mid-Infrared Observations from *MSX*

The shell was the subject of a pointed observation by the *MSX* satellite, which provided images at four mid-infrared wave bands. The shell was clearly detected at 8.3 μm (as shown in Fig. 5) and 12.1 μm (Kraemer et al. 2003). It was not detected in the 14.7 and 21 μm bands, but this is most likely due to the lower sensitivity of those bands, as it is clearly present in the 12 and 25 μm bands of *IRAS* and has been seen by both the Infrared Array Camera (IRAC) and the Multiband Imaging Photometer for *Spitzer* (MIPS) (Jorgensen et al. 2006; L. M. Rebull et al. 2006, in preparation). The higher resolution of the 8 μm *MSX* observations compared to *IRAS* reveals complex filamentary structures within

the shell (Kraemer et al. 2003). In particular, there are three bright knots of 8 μm emission, labeled A, B, and C in Figure 5, which also correspond to enhancements in the extinction at those positions.

3. DISCUSSION

3.1. Could HD 278942 Be the Driving Source of the Shell?

The fact that the shell is visible in the 2MASS extinction map and is filled with preferentially heated dust emission tells us that it is a bubble of heated material, enclosed in a colder shell of increased density (visible only on the edges). Based on multiwavelength data, Andersson et al. (2000) suggested that

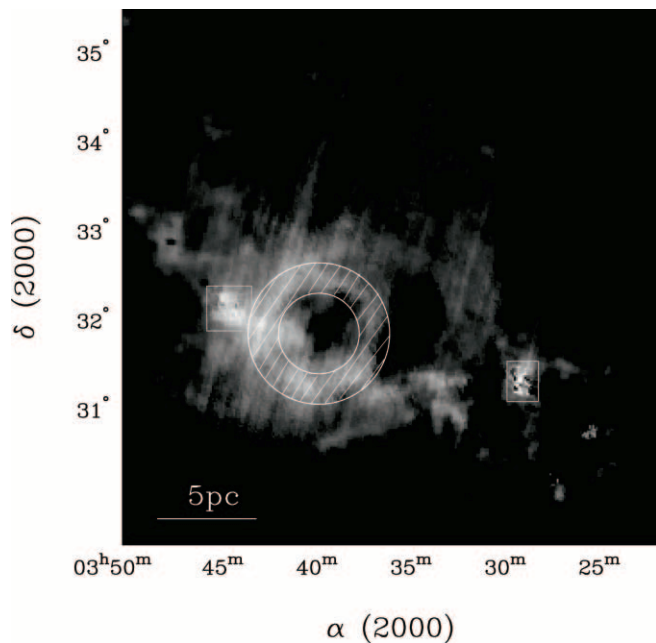


FIG. 6.—*IRAS* extinction map of Perseus. The hatched area indicates the region we define as the shell component; points within the circular region contained within the annulus are defined as inside shell, and points outside the outer circle are defined as the cloud component. The two gray boxes show the small regions around IC 348 (*left*) and NGC 1333 (*right*), which were excluded from the analysis in § 3.2.

the shell was the result of an expanding stellar wind from HD 278942. This is supported by the fact that the shell is filled with H α emission, as is shown in Figure 4.

Historically, the combined effects of the shell and the high reddening toward HD 278942 ($A_V = 7.4$ mag; Andersson et al. 2000) has made spectral classification of the star problematic, with values in the literature ranging from F2 (*Hipparcos*) through B3 III (Černis 1993) to O9.5–B0 V (Andersson et al. 2000). The situation is further complicated by the possibility that HD 278942 may be a photometric B3 III + F5 I binary (Černis 1993). Recent spectra obtained by Steenbrugge et al. (2003) confirm that HD 278942 is most likely an early-to-mid-B star. Assuming a local density n_H of 1 cm^{-3} , such a star could produce an H II region of several parsecs in size (Osterbrock 1989). Given the uncertainty in the star’s spectral classification and the local density, it is therefore plausible that HD 278942 created the 10 pc diameter shell.

3.2. Evidence for Two Dust Populations in Perseus

In order to compare the properties of the shell with other regions of the cloud, we selected by eye an annular region of the *IRAS* column density image that contains all of the shell emission. Figure 6 shows this region as a hatched annulus overlaid on the *IRAS* column density image. In the remainder of the text we refer to the hatched region of the annulus as the shell component, the circular region contained within the annulus as inside shell, and all points in the image that are outside of the annulus as the cloud component. Also shown are two small gray boxes, which indicate the positions of the two young clusters NGC 1333 and IC 348, which we excluded from our analysis.

Our new *IRAS* calibration technique (Schnee et al. 2005) leads to temperature and column density maps that look somewhat different from those presented in Andersson et al. (2000). They interpreted their temperature map as showing that the ring

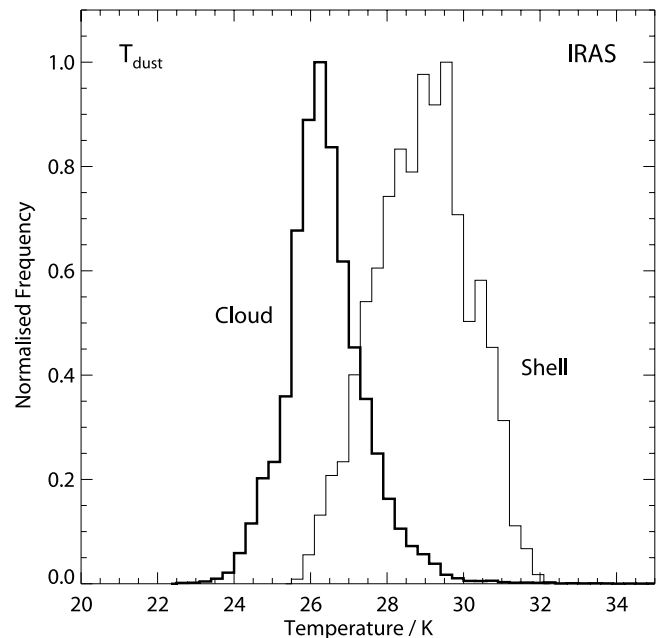


FIG. 7.—Histogram of dust temperature determined from *IRAS* 60 and $100 \mu\text{m}$ emission. The thick line represents the cloud component, while the thin line shows the shell component. Note that small areas containing the young clusters IC 348 and NGC 1333 were excluded (see Fig. 6). The histograms are normalized due to the large difference in the number of points in the two components (65,000 points for the cloud vs. 6800 for the shell component).

is at a temperature minimum of 24 K, with the dust inside the shell at a higher temperature. The fact that they also found the cloud material outside the shell marginally warmer than the shell itself (making the shell a temperature minimum) is probably an artifact of the way they created their temperature map.

We find an average temperature in the shell component of 28.9 K, with a maximum of 32 K. The distribution of temperatures within the shell component and cloud component is shown in Figure 7. It is clear that the shell component is significantly warmer than the molecular cloud material that surrounds it. This is supported by a two-sided Kolmogorov-Smirnov (KS) test, which gives a probability of $< 10^{-5}$ that the two samples are drawn from the same population.

In Figure 8 we show a scatter plot of the color temperature versus column density derived from recalibrated *IRAS* 60 and $100 \mu\text{m}$ emission (Schnee et al. 2005). Three distinct populations are seen in the emission, indicated by the green points (cloud component), red points (shell component), and blue points (inside shell). Clearly, the shell and its interior are warmer and denser on average than the surrounding cloud.

The difference in density can be seen more clearly in the histograms shown in the left panel of Figure 9. The cloud component has a mean extinction of 1.6 mag, while the mean of extinction in the shell component is almost double that (3.1 mag). Again, a two-sided KS test gives a probability of $\ll 10^{-5}$ that the two populations (cloud and shell) are drawn from the same parent population.

Also shown in the right panel of Figure 9 is a histogram of extinction as derived from 2MASS/NICER for the shell component. If we assume that the 2MASS/NICER derived extinction is a better estimate of the “true” column density of material toward any line of sight, then it appears that *IRAS* is systematically overestimating the column density of material in the shell.

Another way to look at this is Figure 10, in which we show a scatter plot of column density derived from *IRAS* against

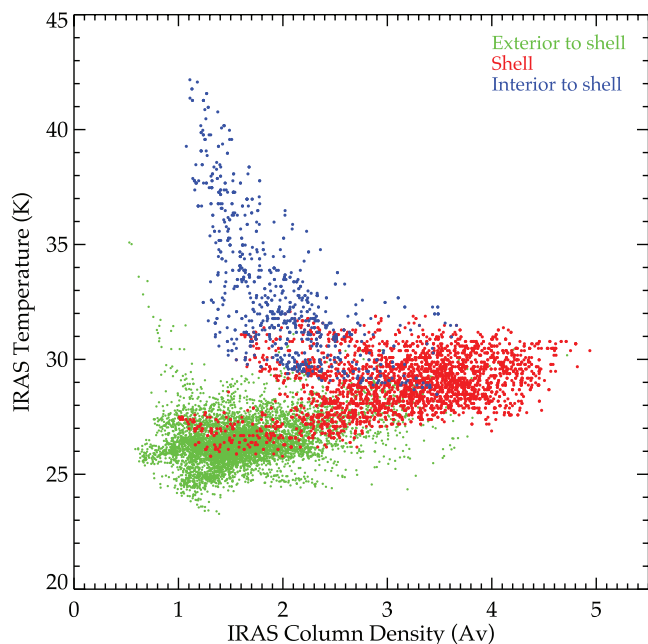


FIG. 8.—Column density vs. temperature derived from *IRAS* 60 and 100 μm emission. Green points indicate cloud component points (i.e., outside the outer circle of the annulus shown in Fig. 6). Red dots indicate points within the hatched annulus (shell component), and blue dots indicate points from the interior of the shell (i.e., inside the inner circle of the annulus).

column density from 2MASS/NICER. A solid line in the figure shows a linear least-squares fit to the data, and the dashed line indicates a 1:1 relation between the two properties. Clearly, the shell component (red points) falls preferentially above both the fitted line and the 1:1 line, again indicating that *IRAS* seems to be overestimating the column density in the shell region.

The “shell” (red) and “cloud” (green) populations seen in Figure 8 are less apparent when we make a similar plot of

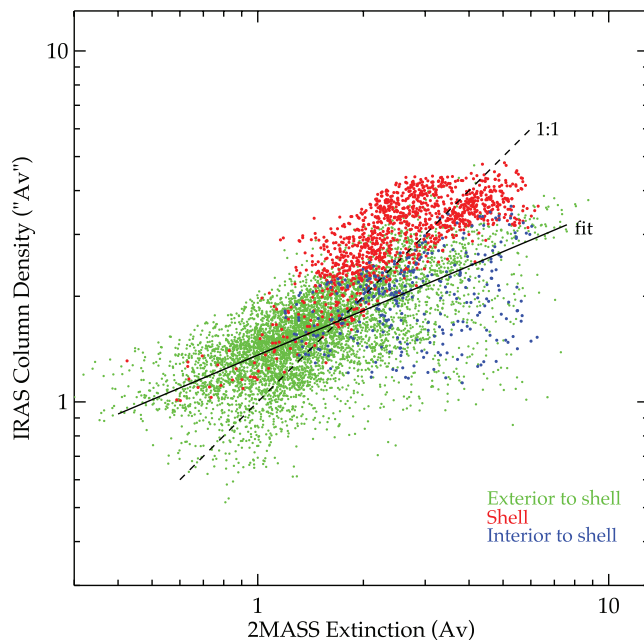


FIG. 10.—*IRAS* column density vs. 2MASS extinction. The dashed line shows a 1:1 relation, and the solid line shows a fit to the data. The data clearly differ from the 1:1 line. Note that for clarity only 10% of the green (cloud component) points are plotted, but the fit is heavily weighted by this component. Symbols are the same as in Fig. 8.

temperature determined from *IRAS* against extinction determined from 2MASS/NICER, as is done in Figure 11. Although still warmer on average, the shell component does not show a significant difference in column density when compared to the cloud component.

We interpret the “high-contrast” appearance of the shell on the *IRAS*-based column density maps as caused by the presence of two different dust populations along the line of sight: the cool

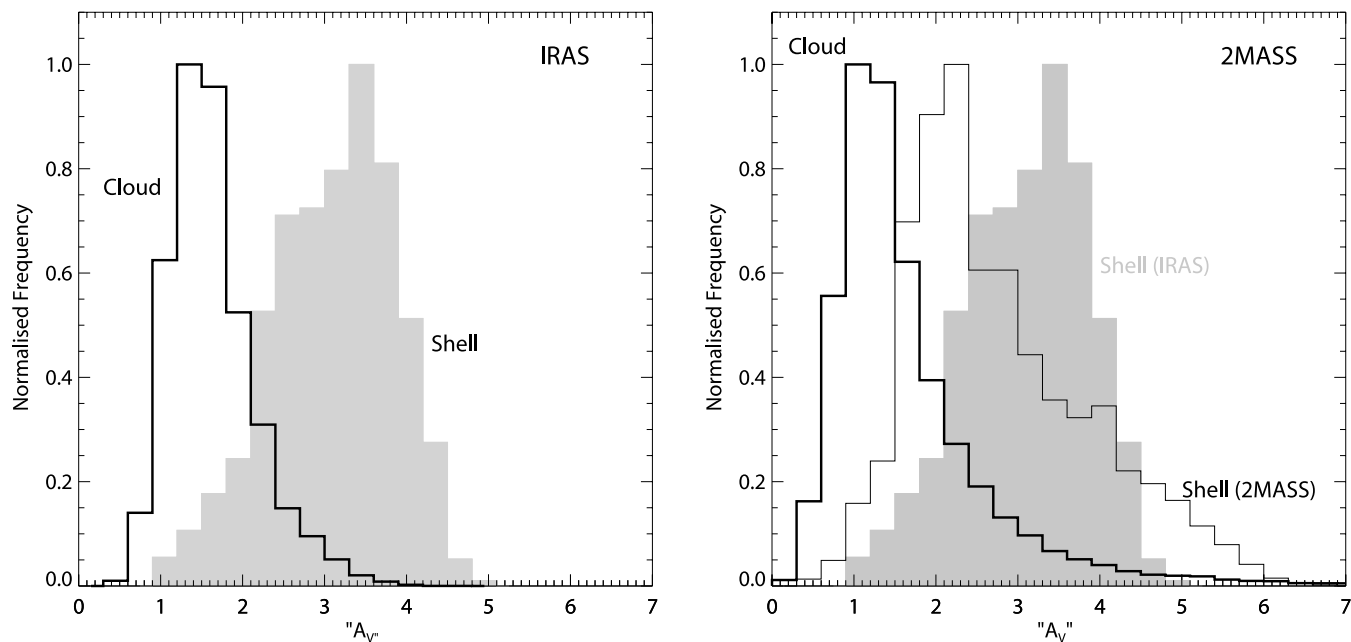


FIG. 9.—Normalized histograms of extinction from *IRAS* and 2MASS/NICER. In both panels, the thick line represents the cloud component, and the gray filled histogram shows the shell component as traced by *IRAS* (hatched region in Fig. 6). The thin line in the right histogram shows the shell component as traced by 2MASS/NICER. Note that small areas containing the young clusters IC 348 and NGC 1333 were excluded in both cases (see Fig. 6) and that the histograms are normalized due to the large difference in the number of points in the two components (65,000 points for the cloud vs. 6800 for the shell component).

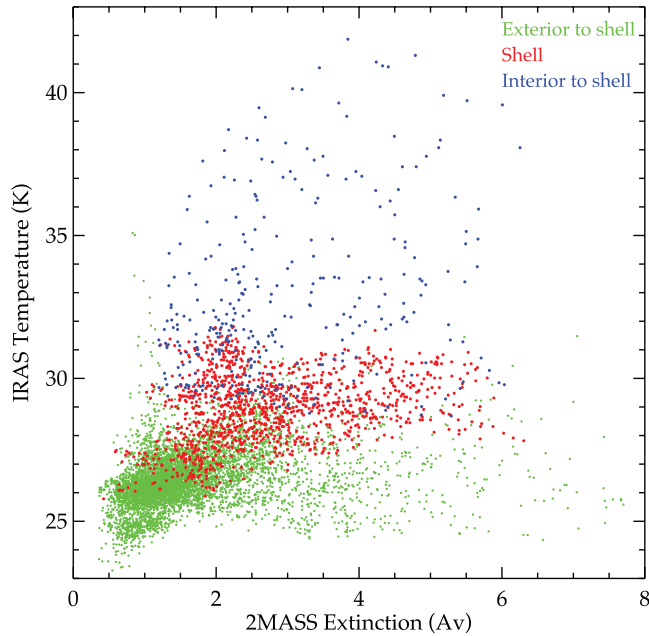


FIG. 11.—Temperature from *IRAS* 60 and 100 μm emission vs. extinction from 2MASS/NICER. Symbols are the same as in Fig. 8.

component associated with the molecular cloud complex, and a warmer component due to the shell. This type of situation was discussed in an appendix of Langer et al. (1989), who showed that the result of assuming a single dust temperature along a line of sight is an *underestimate* of the total optical depth (and hence

column density). However, in this case we know the “true” column density of shell material from the 2MASS/NICER map is in fact less than the column density we determine from *IRAS*; i.e., the line-of-sight dust distribution seems to cause an *overestimate* of the 100 μm opacity within the shell component, as can be seen in the right panel of Figure 9.

An alternative explanation is that our assumption of a uniform dust emissivity coefficient for all of the region is incorrect. It is possible that the grain-size distribution and/or composition of the dust in the shell may be unusual, as it has been processed by the radiation field of the massive star.

The hypothesis of two cloud populations in the direction of Perseus is not new. Ungerechts & Thaddeus (1987) suggested the possibility of two clouds along the line of sight to explain the presence of two distinct velocity components seen in their CO map of Perseus—and in several papers about photometric distances and extinctions toward field stars in the directions of IC 348, NGC 1333, and the dark cloud Barnard 1 (Černis 1990, 1993; Černis & Straizys 2003, hereafter collectively CS), Černis and collaborators have found an apparent jump in extinction toward Perseus at a distance of ~ 140 –160 pc, placing some kind of absorbing material at this distance. They attribute this material to an extension of material from the Taurus molecular cloud complex along the line of sight to Perseus (their suggested morphology is shown in Figure 9 of Černis 1993).

In a study of the optical polarization of background stars Goodman et al. (1990, hereafter GBMM90) found a bimodal distribution of polarization angles in the Perseus region and attributed it to two separate dust distributions along the line of sight, each associated with a different magnetic field orientation. At the time, comparing only to molecular line maps, they could detect

TABLE 1
DISTANCES, EXTINCTIONS, AND POLARIZATIONS OF STARS IN PERSEUS

ID ^a (1)	R.A. (J2000.0) (2)	Decl. (J2000.0) (3)	<i>R</i> (pc) (4)	<i>A_V</i> (mag) (5)	<i>P</i> ^b (%) (6)	Θ (deg) (7)
Stars with <i>A_V</i> < 0.7						
30.....	03 33 04	30 34.5	268	0.21	0.51	87
40.....	03 33 55	31 10.0	310	0.29	1.24*	72
51.....	03 33 41	31 07.9	195	0.37	0.42	80
71.....	03 35 41	30 55.7	254	0.17	0.66	74
72.....	03 35 52	31 15.0	141	0.42	0.34	70
88.....	03 36 36	31 04.5	134	0.25	0.34	110
Stars with <i>A_V</i> > 0.7						
15.....	03 31 54	30 55.8	700	2.33	1.14*	17
24.....	03 32 44	30 30.3	300	2.99	0.21	114
31.....	03 33 10	30 50.3	860	2.18	0.43	143
74.....	03 35 55	31 33.8	440	1.38	1.46*	146
92.....	03 36 42	31 31.1	1430	0.71	1.12*	156
111.....	03 37 33	30 58.9	264	2.47	4.69*	145
112.....	03 37 45	31 07.0	5200	1.24	5.06*	152
124.....	03 38 24	31 12.0	245	3.56	9.14*	150
125.....	03 38 36	31 56.5	340	1.66	1.23*	137
HD 278942	03 39 55	31 55 33.2	207 ^c	7.4 ^{*d,e}	5.9 ^{*d}	154 ^d

NOTES.—Adapted from Tables 1 and 3 of Černis & Straizys (2003). Units of right ascension are hours, minutes, and seconds, and units of declination are degrees, arcminutes, and arcseconds.

^a Notation of CS.

^b Entries shown with an asterisk have polarization percentage >1%.

^c *Hipparcos* (Perryman et al. 1997).

^d Andersson et al. (2000).

^e Contains a significant circumstellar component (Andersson et al. 2000).

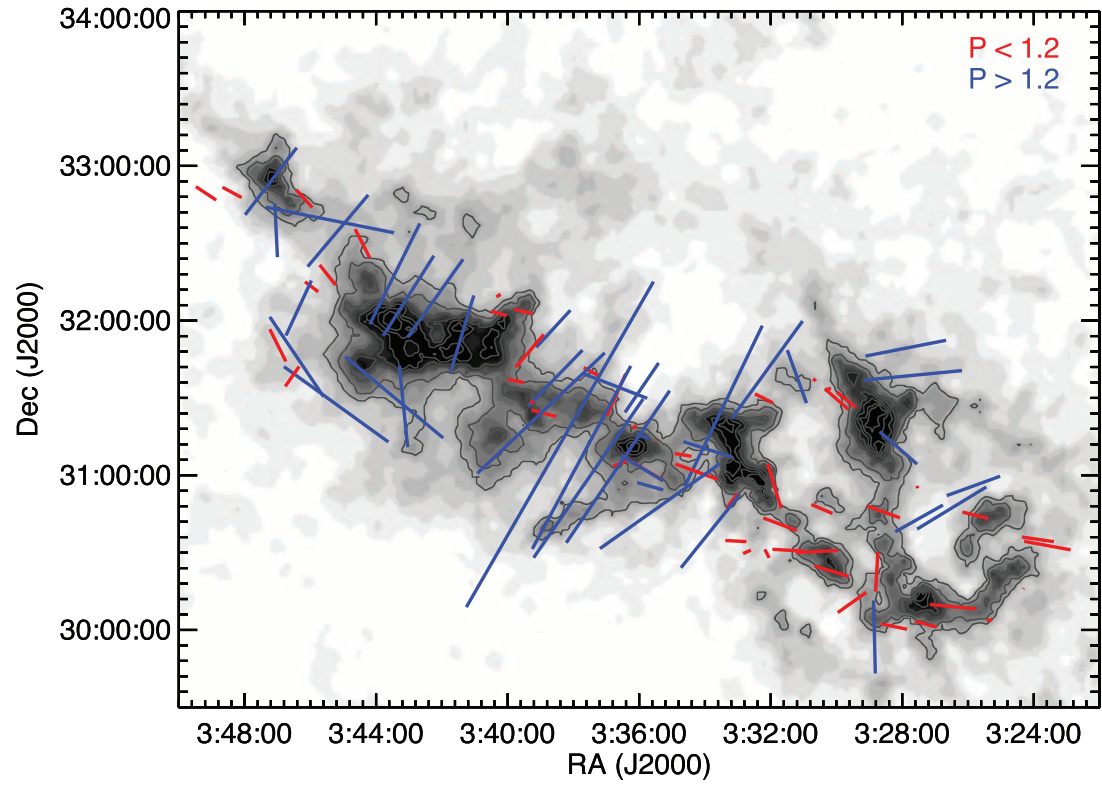
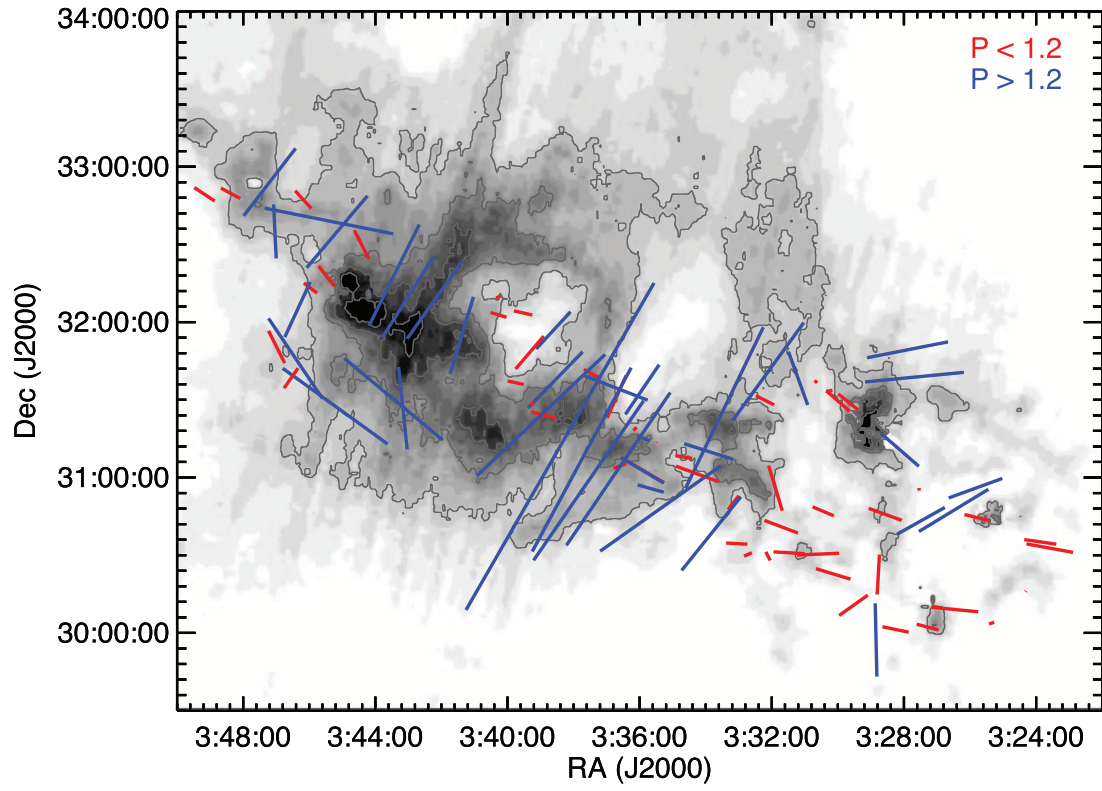


FIG. 12.—*IRAS* column density (*top*) and extinction from 2MASS (*bottom*) overlaid with polarization vectors from GBMM90. Blue vectors have polarization strength $P > 1.2\%$, and red vectors have $P < 1.2\%$. The stronger polarization component (*blue*) appears aligned with the warm dust emission seen in the *IRAS* map, while the weaker component mostly lies along the chain of molecular clouds, most evident in the 2MASS extinction map.

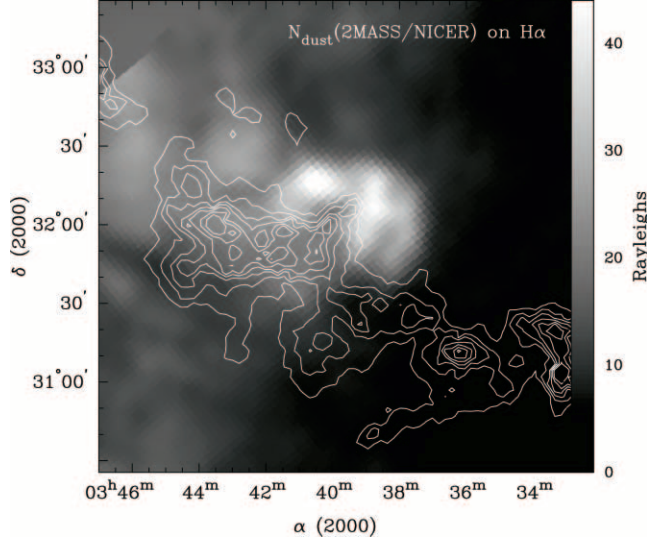


FIG. 13.—H α emission (Finkbeiner 2003; Dennison et al. 1998), overlaid with contours of extinction from 2MASS/NICER. The extinction from the molecular clouds obscures the southwest quadrant of the ionized emission, indicating that the H α emission, and hence the shell, is behind the cloud complex.

no meaningful spatial distinction between the two polarization components.

CS have 18 stars in common with GBMM90; CS were able to determine distances and extinctions for 15 of these, based on photometric spectral typing. The properties of these 15 stars are summarized in Table 1, which is reproduced for the most part from CS. We have split the stars in the table into two groups: those with $A_V < 0.7$ and those with $A_V > 0.7$.

From Table 1, it is clear that the stars with *high* polarization percentage (asterisked entries in column [6] of the table) appear almost exclusively in the *high*-extinction (≥ 0.5 mag) group, while stars with low polarization percentage are more common at lower extinction. The lower extinction stars also tend to be at nearer distances. CS interpreted these results as further evidence for their 140 pc material, proposing that stars with low polarization are located between the 140 pc material and the cloud complex, while the more distant stars show high polarization and high extinction because they are behind two layers of absorbing material (the 140 pc material and the molecular cloud).

In Figure 12 we show polarization vectors from GBMM90 overlaid on our *IRAS* column density and ^{13}CO maps. The weaker polarization component identified by GBMM90 is clearly aligned along the major axis of the molecular cloud as stated in that paper, but on comparison with our new column density maps it now becomes evident that much of the high-polarization-percentage component is aligned with the warm shell and associated arm to the west.

In fact, the polarization strength ($\leq 1.2\%$) measured for the weaker component is typical for nearby molecular clouds (e.g., GBMM90; Bhatt et al. 2004). We therefore propose that the weaker component is due to magnetic fields within the molecular cloud material, while the stronger component is due to a swept-up field associated with the shell material. This is consistent with CS's measurements, as the distances to the low-polarization stars (nonasterisked entries in column [6] of Table 1) place them close to the distance of the molecular cloud complex, while the higher-polarization stars (asterisked entries in column [6] of the table) are generally more distant than 300 pc. Andersson et al. (2000) measured a polarization of $5.9\% \pm 0.03\%$ at a position angle of $154.0^\circ \pm 0.2^\circ$ toward HD 278942, also consistent with its

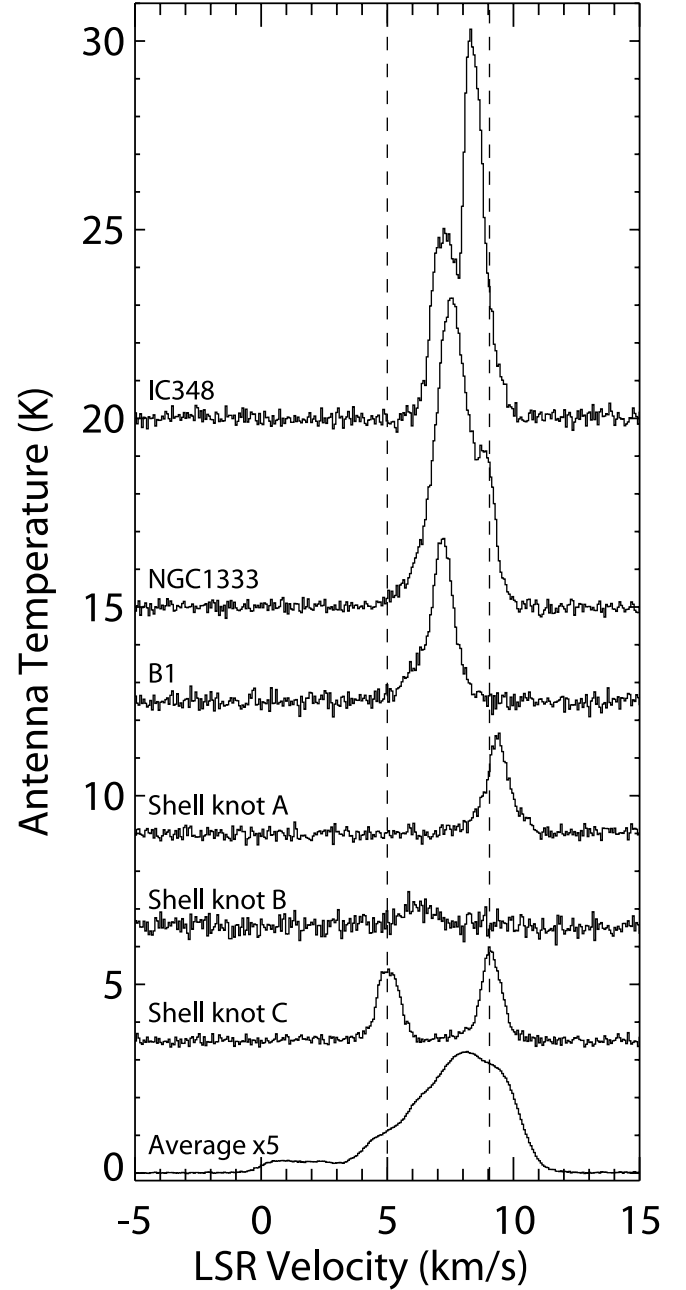


FIG. 14.—“Sampler” of ^{13}CO spectra from the Perseus region. The bottom spectrum shows the mean spectrum of all positions where ^{13}CO was detected at the 5σ level within the boundaries shown in Fig. 3. This spectrum is multiplied by a factor of 4. Shown above the average spectrum are three spectra from the positions of the 8 μm knots labeled A, B, and C in Fig. 5. The component at 5 km s^{-1} in knot C is due to an unusual-looking small feature that appears unconnected either spatially or in velocity to the rest of the cloud complex (see also Fig. 15) and hence may be due to an interaction between the shell and the cloud complex. At the top, three spectra from the position of peak ^{13}CO emission in the known star-forming clumps NGC 1333 ($\alpha_{J2000.0} = 03^{\text{h}}29^{\text{m}}09^{\text{s}}.5$, $\delta_{J2000.0} = +31^{\circ}21'45''$), IC 348 ($\alpha_{J2000.0} = 03^{\text{h}}44^{\text{m}}03^{\text{s}}.9$, $\delta_{J2000.0} = +32^{\circ}04'23''$), and B1 ($\alpha_{J2000.0} = 03^{\text{h}}34^{\text{m}}36^{\text{s}}.0$, $\delta_{J2000.0} = +31^{\circ}23'34''$) are shown for comparison. The dashed lines show the central velocity of the two components of knot C.

polarization being associated with the shell in our scenario (although we note that some fraction of the polarization is thought to be circumstellar).

Although we do not know its distance, the shell cannot be the source of CS's proposed 140 pc material, as it must lie *behind* the molecular cloud complex. We know this, because in Figure 13,

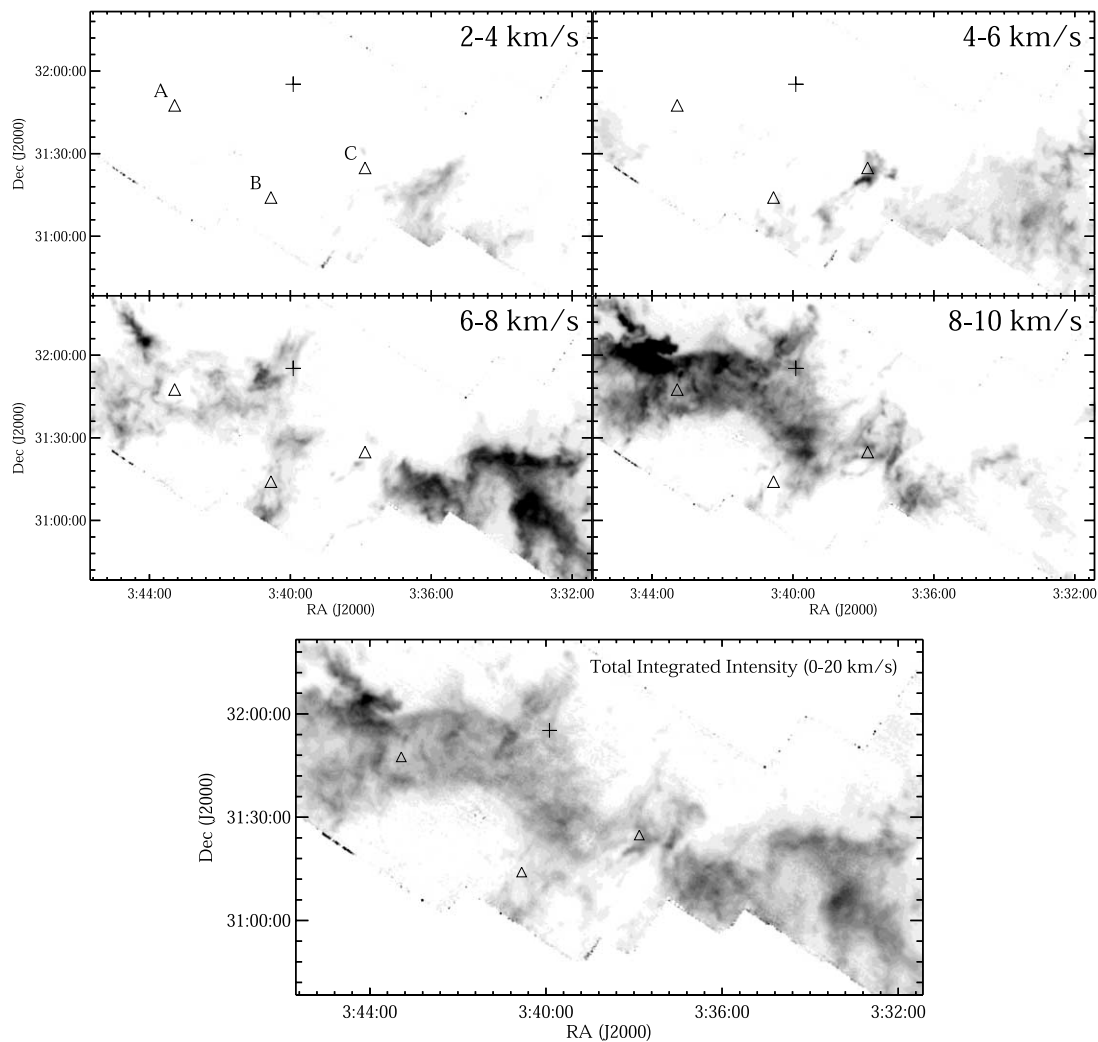


FIG. 15.—*Bottom*: Total integrated ^{13}CO intensity near the shell. The plus sign indicates the position of HD 278942. The three triangles show the positions of the three $8\ \mu\text{m}$ knots that were also indicated in Fig. 5 (A, B, and C, from left to right). *Top panels*: Channel maps in intervals of $2\ \text{km s}^{-1}$ of the same region. Velocities are given in the top right corner of each panel. The bright feature at the center of the $4\text{--}6\ \text{km s}^{-1}$ channel (*top right*) is due to the $5\ \text{km s}^{-1}$ component seen in the spectrum at the position of the $8\ \mu\text{m}$ knot C (Fig. 14), but is not physically connected to the emission associated with the molecular clouds at similar velocities.

which shows contours of extinction from 2MASS/NICER overlaid on the $\text{H}\alpha$ image, a finger of extinction (*contours*) is exactly coincident with a dark “shadow” to the southeast in the $\text{H}\alpha$ emission. The same shadow can be seen in the 1907 photograph in Barnard’s Atlas (Barnard 1927), against a circular shaped nebulosity that is located within the circumference of the shell. This would place the shell behind at least the eastern end of the Perseus molecular cloud complex and therefore more distant than $260 \pm 20\ \text{pc}$, the distance to IC 348 (Černis 1993) that is embedded in that portion of the molecular cloud.⁶ We also do not believe that the shell could be far behind the molecular cloud complex, as several of the more highly polarized stars in Table 1 have distances $\lesssim 300\ \text{pc}$.

3.3. Is the Shell Impacting the Molecular Cloud?

The final piece of the puzzle of the Perseus shell is whether or not it is interacting with the molecular cloud. In earlier sections

⁶ This makes either the distance determination to HD 278942 or its association with the shell somewhat problematic, as its *Hipparcos* distance of $207 \pm 52\ \text{pc}$ (Perryman et al. 1997; Andersson et al. 2000) would place it on the near side of the cloud containing IC 348, while its high reddening and polarization would suggest it is behind a significant column of dense material.

we argue that it is likely to be located behind but still close to the cloud complex. The most compelling evidence for an interaction is given by a comparison of the *MSX* $8\ \mu\text{m}$ image with extinction from 2MASS, as is shown in Figure 5. The shell is clearly detected in $8\ \mu\text{m}$ emission, and in particular has three bright “knots” of emission, labeled A, B, and C in Figure 5.⁷ An extinction of $A_V \gtrsim 100$ is required to make the cloud opaque at $8\ \mu\text{m}$, so the bright knots are likely to be real and not just a result of varying extinction in front of the emission. In fact, the three bright knots are spatially coincident with slight enhancements in the extinction, as indicated by the contours on Figure 5. Emission in the $8\ \mu\text{m}$ band of *MSX* has been modeled as a combination of graybody dust emission and emission from the unidentified infrared bands (UIBs), usually attributed to polycyclic aromatic hydrocarbons (PAHs) excited in shocks (e.g., Ghosh & Ojha 2002), and hence the spatial coincidence between the $8\ \mu\text{m}$ knots and the extinction enhancements is most easily explained by a layer of swept-up material in front of a shock, providing compelling evidence for an interaction. Further evidence is seen in the ^{13}CO emission, in which the spectrum at knot C shows a

⁷ See also Kraemer et al. (2003) for images at all four *MSX* bands.

strong second component at 5 km s^{-1} (Fig. 14), well separated spatially from emission due to the molecular clouds at those velocities (Fig. 15). The second component is blueshifted with respect to the “ambient” molecular gas, consistent with an interaction with the front side of an expanding shell.

CO spectra in the Perseus region are extremely complex and confused, with a velocity gradient of almost 10 km s^{-1} across the cloud and multiply peaked, optically thick lines throughout. We have attempted to make ^{12}CO observations of the top half of the shell, where contamination from the molecular clouds should be low in order to perform a more detailed kinematical analysis of the shell, but as can be seen from the 2MASS/NICER extinction data, the column density there is low, and we have been unable to detect ^{12}CO at sufficient sensitivity to enable such an analysis.

By assuming a gas-to-dust ratio N_{H}/A_V , we can calculate the mass of material in the shell from the 2MASS extinction map, using the relation presented by Dickman (1978),

$$M = (\alpha d)^2 \mu \frac{N_{\text{H}}}{A_V} \sum_i A_V(i), \quad (1)$$

where α is the angular size of a map pixel, d is the distance (300 pc), μ is the mean molecular weight corrected for helium abundance, and $N_{\text{H}}/A_V = 1.87 \times 10^{21} \text{ cm}^{-2} \text{ mag}^{-1}$ (Savage & Mathis 1979), although this number could be higher by a factor of ~ 2 (see, e.g., Goodman & Heiles 1994). Due to the contamination from cloud emission in the lower half of the ring, we calculated the mass in the top half of the shell and scaled this by a factor of 2 to estimate a total mass of the material in the shell of $760 M_{\odot}$. If we assume we are seeing the limb-brightened edge of a complete spherical shell, then the total mass M_{TOT} that such a shell would contain is given by

$$M_{\text{TOT}} = M_{\text{RING}} \left[\frac{R_2^3 - R_1^3}{(R_2^2 - R_1^2)^{3/2}} \right], \quad (2)$$

where M_{RING} is the mass enclosed within the two-dimensional annulus indicated in Figure 6, and R_1 and R_2 are the inner and outer radius of that annulus, respectively. In this case $R_1 = 2.05$ and $R_2 = 4.29$ pc ($d = 300$ pc), leading to a total mass of the shell of $1000 M_{\odot}$. Assuming a typical B star lifetime of 8 Myr and a radius of 4.3 pc gives a time-averaged expansion velocity of 0.5 km s^{-1} for the shell, and a total outward momentum of $520 M_{\odot} \text{ km s}^{-1}$, much less than $10^5 M_{\odot} \text{ km s}^{-1}$ we would estimate based on the properties of the central star (see eq. [18] of Matzner 2002). This would suggest that the shell is in the process of merging with the background gas, in which case it is surprising to see such a coherent ring. This discrepancy could be explained if the shell was initially expanding more quickly into

a higher density material. For instance, the same diameter could be reached in 1 Myr with an expansion velocity of 4 km s^{-1} .

4. SUMMARY

By combining our reanalysis of ISSA data (Schnee et al. 2005) with data from the COMPLETE Survey of Star-Forming Regions (Ridge et al. 2006) and archival $\text{H}\alpha$ and mid-IR observations, we have made a detailed study of the warm dust shell in Perseus that was first reported by Pauls & Schwartz (1989).

1. A comparison of the temperature and extinction derived from *IRAS* 60 and $100 \mu\text{m}$ emission shows two distinct dust populations in the Perseus region. The two populations are clearly spatially separated, with the warmer population being associated with the shell.

2. The shell is also detected, but at much lower contrast, in an extinction map of the same region constructed by applying the NICER algorithm (Lombardi & Alves 2001) to 2MASS (Ridge et al. 2006). This indicates that the shell is not as significant a column density feature as one would infer from the *IRAS* map. It dominates the *IRAS* column density map because it is warm.

3. The shell is spatially coincident with, and hence may be the source of the high-polarization component of, the bimodal distribution of polarizations found in the region by GBMM90. If this is the case, then this would be the first observation of a swept-up magnetic field on ~ 10 pc scales.

4. The combination of *IRAS*, *MSX*, 2MASS/NICER, and ^{13}CO data suggests that the shell is located behind the molecular cloud containing the star-forming cluster IC 348, and there is significant circumstantial evidence that it is interacting with the cloud complex.

5. We reiterate previous conclusions (Arce & Goodman 1999a, 1999b; Cambr sy et al. 2001; Schnee et al. 2005) that care should be taken when using *IRAS* to determine the extinction in the direction of complex regions such as star-forming molecular clouds, as variations in dust temperature along the line of sight can introduce substantial bias toward warm dust features.

This research has made use of the NASA/IPAC Infrared Science Archive, which is operated by the Jet Propulsion Laboratory, California Institute of Technology, under contract with the National Aeronautics and Space Administration; and data products from the Two Micron All Sky Survey, which is a joint project of the University of Massachusetts and the Infrared Processing and Analysis Center/California Institute of Technology, funded by the National Aeronautics and Space Administration and the National Science Foundation. We acknowledge the use of NASA’s SkyView facility (<http://skyview.gsfc.nasa.gov>) located at NASA’s Goddard Space Flight Center. FCRAO is supported by NSF grant AST 02-28993.

REFERENCES

- Andersson, B. G., Wannier, P. G., Moriarty-Schieven, G. H., & Bakker, E. J. 2000, *AJ*, 119, 1325
 Arce, H. G., & Goodman, A. A. 1999a, *ApJ*, 512, L135
 ———. 1999b, *ApJ*, 517, 264
 Aspin, C., Sandell, G., & Russell, A. P. G. 1994, *A&AS*, 106, 165
 Barnard, E. 1927, *A Photographic Atlas of Selected Regions of the Milky Way*, ed. E. Frost & M. Calvert (Washington: Carnegie Institute)
 Bhatt, H. C., Maheswar, G., & Manoj, P. 2004, *MNRAS*, 348, 83
 Cambr sy, L., Boulanger, F., Lagache, G., & Stepnik, B. 2001, *A&A*, 375, 999
 Cernis, K. 1990, *Ap&SS*, 166, 315
 ———. 1993, *Baltic Astron.*, 2, 214
 Cernis, K., & Straizys, V. 2003, *Baltic Astron.*, 12, 301
 Dennison, B., Simonetti, J. H., & Topasna, G. A. 1998, *Publ. Astron. Soc. Australia*, 15, 147
 de Zeeuw, P. T., Hoogerwerf, R., de Bruijne, J. H. J., Brown, A. G. A., & Blaauw, A. 1999, *AJ*, 117, 354
 Dickman, R. L. 1978, *AJ*, 83, 363
 Evans, N. J., et al. 2003, *PASP*, 115, 965
 Fiedler, R., Pauls, T., Johnston, K. J., & Dennison, B. 1994, *ApJ*, 430, 595

- Finkbeiner, D. P. 2003, *ApJS*, 146, 407
- Ghosh, S. K., & Ojha, D. K. 2002, *A&A*, 388, 326
- Goodman, A. A., Bastien, P., Menard, F., & Myers, P. C. 1990, *ApJ*, 359, 363 (GBMM90)
- Goodman, A. A., & Heiles, C. 1994, *ApJ*, 424, 208
- Herbig, G. H., & Jones, B. F. 1983, *AJ*, 88, 1040
- Jorgensen, J. K., et al. 2006, *ApJ*, in press (astro-ph/0603547)
- Kraemer, K. E., Shipman, R. F., Price, S. D., Mizuno, D. R., Kuchar, T., & Carey, S. J. 2003, *AJ*, 126, 1423
- Lada, E. A., & Lada, C. J. 1995, *AJ*, 109, 1682
- Ladd, E. F., Lada, E. A., & Myers, P. C. 1993, *ApJ*, 410, 168
- Langer, W. D., Wilson, R. W., Goldsmith, P. F., & Beichman, C. A. 1989, *ApJ*, 337, 355
- Lombardi, M., & Alves, J. 2001, *A&A*, 377, 1023
- Luhman, K. L., Stauffer, J. R., Muench, A. A., Rieke, G. H., Lada, E. A., Bouvier, J., & Lada, C. J. 2003, *ApJ*, 593, 1093
- Matzner, C. D. 2002, *ApJ*, 566, 302
- Miville-Deschênes, M.-A., & Lagache, G. 2005, *ApJS*, 157, 302
- Osterbrock, D. E. 1989, *Astrophysics of Gaseous Nebulae and Active Galactic Nuclei* (Mill Valley: University Science Books)
- Pauls, T., & Schwartz, P. R. 1989, in *The Physics and Chemistry of Interstellar Molecular Clouds*, ed. G. Winnewisser & T. J. Armstrong (Berlin: Springer), 225
- Perryman, M. A. C., et al. 1997, *A&A*, 323, L49
- Ridge, N. A., et al. 2006, *AJ*, 131, 2921
- Savage, B. D., & Mathis, J. S. 1979, *ARA&A*, 17, 73
- Schnee, S. L., Goodman, A. A., Li, J. G., & Ridge, N. A. 2005, *ApJ*, 634, 442
- Steenbrugge, K. C., de Bruijne, J. H. J., Hoogerwerf, R., & de Zeeuw, P. T. 2003, *A&A*, 402, 587
- Ungerechts, H., & Thaddeus, P. 1987, *ApJS*, 63, 645
- Wood, D. O. S., Myers, P. C., & Daugherty, D. A. 1994, *ApJS*, 95, 457